Novel approaches for direct exoplanet imaging: Theory, simulations and experiments

Por, E.H.

Citation

Por, E. H. (2020, December 11). *Novel approaches for direct exoplanet imaging: Theory, simulations and experiments*. Retrieved from https://hdl.handle.net/1887/138516

Author: Por, E.H.
Title: Novel approaches for direct exoplanet imaging: Theory, simulations and experiments
Issue date: 2020-12-11

Chapter 3

The Single-mode Complex Amplitude Refinement (SCAR) coronagraph

I. Concept, theory and design

Adapted from
E. H. Por and S. Y. Haffert (2020), A&A 635, A55

Context The recent discovery of an Earth-mass exoplanet around the nearby star Proxima Centauri provides a prime target for the search for life on planets outside our solar system. Atmospheric characterization of these planets has been proposed by blocking the starlight with a stellar coronagraph and using a high-resolution spectrograph to search for reflected starlight off the planet.

Aims Due to the large flux ratio and small angular separation between Proxima b and its host star ($\lesssim 10^{-7}$ and $\lesssim 2.2\lambda/D$ respectively; at 750nm for an 8m-class telescope) the coronagraph requires high starlight suppression at extremely-low inner working angles. Additionally, it must operate over a broad spectral bandwidth and under residual telescope vibrations. This allows for efficient use of spectroscopic post-processing techniques. We aim to find the global optimum of an integrated coronagraphic integral-field spectrograph.

Method We present the Single-mode Complex Amplitude Refinement (SCAR) coronagraph that uses a microlens-fed single-mode fiber array in the focal plane downstream from a pupil-plane phase plate. The mode-filtering property of the single-mode fibers allows for the nulling of starlight on the fibers. The phase pattern in the pupil plane is specifically designed to take advantage of this mode-filtering capability. Second-order nulling on the fibers expands the spectral bandwidth and decreases the tip-tilt sensitivity of the coronagraph.

Results The SCAR coronagraph has a low inner working angle ($\sim 1\lambda/D$) at a contrast of $< 3 \times 10^{-5}$ for the six fibers surrounding the star using a sufficiently-good adaptive optics system. It can operate over broad spectral bandwidths ($\sim 20\%$) and delivers high throughput ($> 50\%$ including fiber injection losses). Additionally, it is robust against tip-tilt errors ($\sim 0.1\lambda/D$ rms). We present SCAR designs for both an unobstructed and a VLT-like pupil.

Conclusions The SCAR coronagraph is a promising candidate for exoplanet detection and characterization around nearby stars using current high-resolution imaging instruments.

3.1 Introduction

The discovery of many rocky exoplanets around stars (Borucki et al., 2011) has prompted the radial velocity search of the closest and brightest ones. This led to the discovery of a terrestrial exoplanet in the habitable zone around Proxima Centauri (Anglada-Escudé et al., 2016). This planet does not transit its host star (Kipping et al., 2017), making transit spectroscopy impossible. Proxima b however has an angular separation in quadrature of $\sim 2.2\lambda/D$ at 750nm for an 8m-class telescope, making a spatially resolved imaging approach feasible. Lovis et al. (2017) explores the possibility of coupling the high-contrast imager SPHERE (Beuzit et al., 2008) with the high-resolution spectrograph ESPRESSO (Pepe et al., 2010). The implementation of the coronagraph was left as an open question. Here we show a new type of coronagraph that will enable a combination of SPHERE and a high-resolution spectrograph to successfully observe Proxima b.

With the advent of extreme adaptive optics systems (xAO), such as SPHERE (Beuzit et al., 2008), GPI (Macintosh et al., 2014) and SCExAO (Jovanovic et al., 2015), direct detection has taken some major steps forward. These systems create a diffraction-limited point spread function (PSF), which allows for the use of coronagraphy to enhance the contrast of observations. Coronagraphs need to suppress stellar light at the location of the planet, while having high throughput for the planet itself. Additionally, they need to operate over a broad wavelength range and in the presence of residual telescope aberrations, both static and dynamic. Telescope vibrations in particular turned out to be a major concern for these high contrast imaging instruments (Fusco et al., 2016). The performance of pupil-plane-only coronagraphs is independent of telescope pointing, making telescope vibrations less of a concern. An inherent disadvantage of pupil-plane coronagraphs is that the coronagraphic throughput loss is the same for the star and the planet. Therefore designs of pupil-plane coronagraphs that reach high contrasts or extremely-low inner working angles have an intrinsically low throughput. As a result, coronagraphs combining focal-plane and pupil-plane optics often outperform pupil-plane-only coronagraphs at extremely-low inner working angles (Mawet et al., 2012). For example, an apodizing phase plate (APP) with an annular dark zone optimized from $1.2\lambda/D$ to $2.3\lambda/D$ for a contrast of 10^{-4} has a Strehl ratio (ie. planetary throughput) of 0.13%. The APP optimization was performed following Por (2017).

Even with the best adaptive optics systems, residual aberrations will always limit the raw contrast of ground-based observations to $\sim 10^{-6}$ to 10^{-7} (Guyon, 2005). Currently however, observations are limited by the non-common-path errors between the wavefront sensor and science camera, creating quasi-static speckles in the focal-plane. These speckles amplify atmospheric residuals (Aime & Soummer, 2004) and are notoriously hard to predict. The raw contrast in the intensity image provided by the coronagraphic system is often enhanced by post-processing techniques to form the final contrast curve of the observation. Diversity of some kind is often used to calibrate the instrument itself. Angular diversity (Marois et al., 2006) uses the rotation of the sky with respect to the instrument and has provided excellent results. A recent development in this field uses the diversity in radial velocities of the star and the planet: stellar-light speckles still retain the radial velocity of the star, while the planet appears at a different velocity altogether. Cross-correlation techniques on high-resolution spectroscopy (Konopacky et al., 2013; Riaud & Schneider, 2007; Sparks & Ford, 2002) combined with coronagraphy (Kawahara et al., 2014; Snellen et al., 2015; Wang et al., 2017) show great promise. They provide dayside spectroscopy of τ Boötis b (Brogi et al., 2012) and even the first measurement of planetary spin (Snellen et al., 2014).

Integration of both coronagraphy and high-resolution spectroscopy into a single concept has only recently been attempted. Mawet et al. (2017) use a fiber injection unit in the focal-plane downstream from a conventional vortex coronagraph. A single-mode fiber was centered around the planet and the stellar light speckles were removed using active speckle control algorithms. While this setup does allow for transportation of the light to a dedicated high-resolution spectrograph, it does not optimally combine both methods. A system for which all components are optimized simultaneously is always better than, or at least as good as, a system for which each component is optimized separately. In this paper we allow the coronagraph design to depend on the single-mode fibers in the focal plane. This allows for more freedom in the design process and provides better planetary coronagraphic throughput as those modes filtered out by the fiber injection unit do not need to be suppressed by the upstream coronagraph. The increase in throughput can be quite significant. For example, optimizing a SCAR coronagraph with an operating angular separations from $1\lambda/D$ to $2.5\lambda/D$ yields a throughput of $\sim 54\%$, compared to the $\sim 0.13\%$ of the corresponding APP mentioned above.

The schematic layout of the proposed coronagraph is shown in Figure 3.1. The SCAR coronagraph uses a phase plate in the pupil plane to

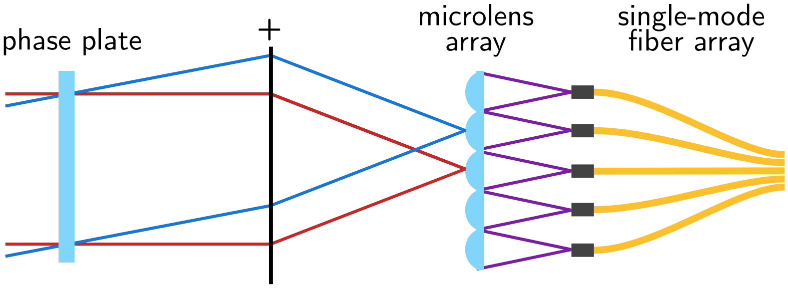

Figure 3.1: Schematic layout of the proposed system. The phase plate located in the pupil-plane alters the PSF that is imaged on the microlens array. Each microlens focus is imaged on a single-mode fiber. An off-axis source will be spatially separated in the focal-plane and its Airy core will fall on a different microlens.

alter the PSF. The light is then focused on the microlens array which focuses the light into the single-mode fiber array. This provides additional filtering of the incoming starlight. The starlight is nulled on off-axis fibers, while light is let through in the center fiber. This means that the light from an off-axis companion, of which the PSF is the same as that of the star, will be let through by the off-axis fiber on which it is centered. In this paper, we aim to provide an overview of the principle and optimization behind the SCAR coronagraph.

Interestingly, the use of single-mode fibers for coronagraphy is not new. Haguenauer & Serabyn (2006) already propose using a single-mode fiber to null the star by using a π phase shift on part of the pupil. Martin et al. (2008) develop this further and Hanot et al. (2011) finally put this system on sky. These applications of single-mode fibers for coronagraphy were based on interferometry. Mawet et al. (2017) is the first to put single-mode fibers behind a conventional coronagraph.

In Sect. 3.2 we describe nulling on single-mode fibers, extend the fiber injection unit to use multiple single-mode fibers and show the coronagraphic capabilities and throughput of such a system. In Sect. 5.5 we use an apodizing phase plate coronagraph to expand the spectral bandwidth and decrease the tip-tilt sensitivity. In Sect. 3.4 we describe the throughput, inner working angle, chromaticity and sensitivity to aberrations of this new system. We conclude with Sect. 3.6.

3.2 Modal filtering using single-mode fibers

3.2.1 Nulling in single-mode fibers

The coupling efficiency η_{sm} of light into a single-mode fiber can be calculated by the projection of the input electric field E_{in} onto the mode of the fiber E_{sm} as

$$\eta_{\mathrm{sm}} = \frac{\left|\int E_{\mathrm{in}}^{*} E_{\mathrm{sm}} \mathrm{d}A\right|^2}{\int |E_{\mathrm{in}}|^2 \mathrm{d}A \ \int |E_{\mathrm{sm}}|^2 \mathrm{d}A}, \tag{3.1}$$

where the integration is done over all space. The fiber mode E_{m} can be calculated using waveguide theory and the geometry of the fiber in question, but in this paper we use the Gaussian approximation (Marcuse, 1978)

$$E_{\mathrm{sm}}(r) = \exp\left[-\frac{r^2}{w^2}\right] \tag{3.2}$$

where r is the distance from the center, and $2w$ is the mode field diameter of the fiber. We see that the coupling efficiency $\eta_{\mathrm{sm}} \leq 1$ for all input fields and that maximum coupling is only attained when E_{in} matches the fiber mode.

Suppose now that we put a single-mode fiber in the focal plane of a telescope, with its mode field diameter matched to that of the Airy core of the PSF. Using Equation 3.1 we can calculate the coupling efficiency $\eta_s(\mathbf{x})$ of the star as a function of focal-plane position x. We can do the same thing for the planet, yielding $\eta_p(\mathbf{x}, \mathbf{x}_0)$ where $\mathbf{x}_0$ is the location of the planet. The raw contrast at the fiber output can be written as

$$C_{\mathrm{raw}}(\mathbf{x}, \mathbf{x}_0) = \frac{\eta_{\mathrm{s}}(\mathbf{x})}{\eta_{\mathrm{p}}(\mathbf{x}, \mathbf{x}_0)}. \tag{3.3}$$

When the fiber is centered around the planet, ie. $\mathbf{x} = \mathbf{x}_0$, the electric field of the planet will couple efficiently into the fiber, as the Airy core is closely matched to the Gaussian fiber mode. The electric field of the star at this position will however consist of Airy rings. These will be smaller, not only in intensity but also spatially so that around two Airy rings will be visible on the fiber face. This is possible as the Airy core itself has a size of $\sim 1\lambda/D$ full-width half-maximum (FWHM), while the Airy rings are sized $\sim 0.5\lambda/D$ FWHM. As neighboring Airy rings have opposite phase, the light from the two Airy rings will (partially) cancel each other in the projection integral of Eq. 3.1, resulting in a lower stellar throughput. This nulling

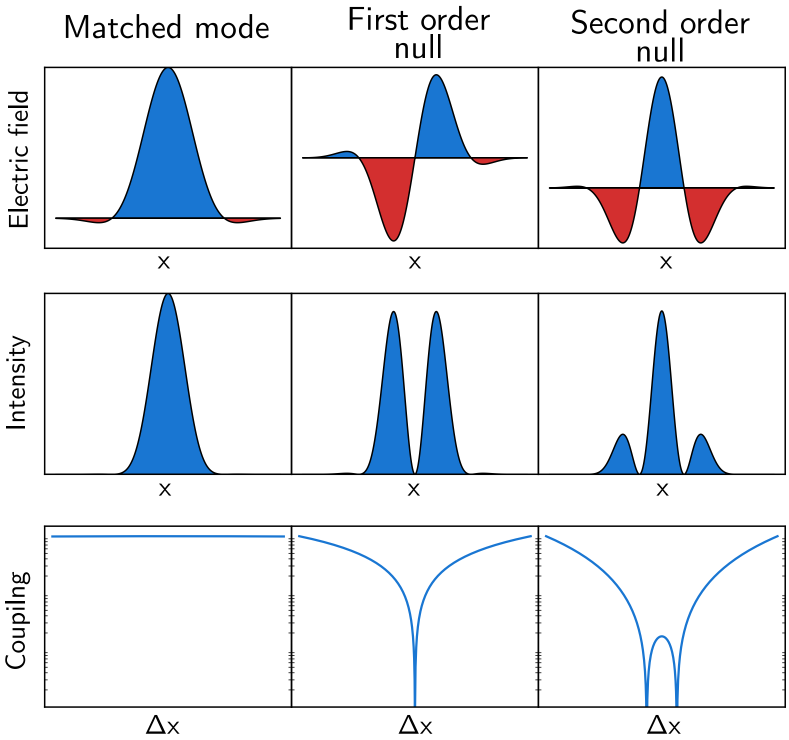

Figure 3.2: Coupling into a single-mode fiber with a (a) matched electric field, (b) first order null and (c) second order null. The first row shows the electric field projected onto the fiber. The second row shows the intensity on the fiber face. The third row shows the coupling efficiency for off-center fibers. The matched mode couples well into the fiber, even for small off-center positions. The first-order null has no throughput: its odd electric field ensures a zero overlap integral in Eq. 3.1. Off-center positions however still transmit because the odd structure is lost. The second-order employs an even electric field where the contribution of the central peak is canceled by the two sidebands. This creates a much broader null when decentering the fiber.

provides an additional contrast enhancement not possible with multimode fibers. Fig. 3.2 illustrates this graphically in columns one and two.

Column three in Fig. 3.2 shows an alternative null structure. This second-order null balances the contribution of the core with its two sidebands. This has the effect of broadening the null for decenter as the loss in overlap with one of the sidebands is compensated by the increase in overlap with the other. In this case we have essentially split the second-order null into two first-order null by subtracting a tiny fraction of the matched mode. This gives a characteristic double dip in the coupling curve and broadens the null even more by raising the coupling between the two first-order nulls. This coupling at the center must be kept below the design coupling.

This second-order null is the basis for the SCAR coronagraph. For comparison with existing coronagraph implementations, we define the "relative integration time" as the ratio between the integration time for unresolved imaging and coronagraphic imaging to reach a predefined signal-to-noise ratio. This can be expressed in the star and planet throughput as

$$\frac{\Delta T_{\text{coronagraphic}}}{\Delta T_{\text{unresolved}}} = \frac{\eta_s(\mathbf{x})}{\eta_p^2(\mathbf{x}, \mathbf{x}_0)}. \tag{3.4}$$

This metric takes into account both the raw contrast and planet throughput of the coronagraph. Noise sources other than photon noise were ignored in this respect. As these only become important for small planet throughputs, we will show both the relative integration time η_s/η_p^2 and the planet throughput η_p.

3.2.2 Single-mode fiber arrays using microlenses

To cover the field of view around a star, we need to fill the focal plane with single-mode fibers. This means that the fibers are impractically close together. A more reasonable solution is to use a microlens array with a single-mode fiber in each focus, as shown by Corbett (2009). Each fiber face now contains a strongly spatially-filtered telescope pupil. The corresponding focal-plane mode for each fiber can be recovered by back-propagating the fiber mode to the focal plane. An example of such a mode is shown in Fig. 3.3. The amplitude of this back-propagated mode is still Gaussian in amplitude. In phase however, it is flat within the central lenslet, but picks up a phase gradient on off-axis lenslets: light hitting off-axis lenslets need to have a huge tilt to still couple into the central fiber. We denote this off-axis contribution as lenslet crosstalk, and it is taken into account in every optimization and calculation done in this paper.

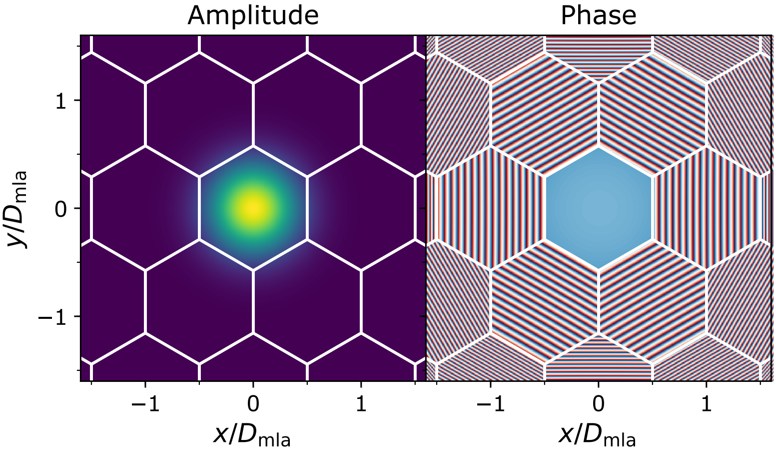

Figure 3.3: Backpropagated mode of a single-mode fiber to the microlens array surface. Conceptually our microlens array and single-mode fiber can still be thought of as focal-plane electric field filtering using this modified mode. The mode is still Gaussian on the central microlens, but picks up an additional tilt on off-axis microlenses: on those microlenses the light needs to have a huge tilt to be propagated into the central fiber.

The throughput of the single-mode fiber array depends on the position of the object and the mode field diameter of the fibers. Figure 3.4 shows the throughput for a clear aperture with slices through the best and worst-case position angles. The throughput is dominated by the lenslet closest to the center of the PSF and is only weakly dependent on the mode field diameter around the optimal value. Additionally, at each position in the focal plane, the optimal value of the mode field diameter is the same, simplifying implementation.

Figure 3.5 shows the throughput of an off-axis lenslet as a function of microlens diameter, while keeping the PSF centered around the on-axis lenslet. We can clearly see that at a diameter of $\sim 1.28\lambda/D$ no stellar light is transmitted by the fiber. This contrast is solely the result of the mode-filtering property of the single-mode fiber: if we were to use multimode fibers instead, the contrast would still be $\sim 3 \times 10^{-2}$ at this point. The nulling can be classified as first order: only where the electric field of the Airy core and the first Airy ring exactly cancel do we see the contrast reduction. Moving the PSF only slightly already destroys this nulling.

Since the PSF changes in size with wavelength, the throughput of an

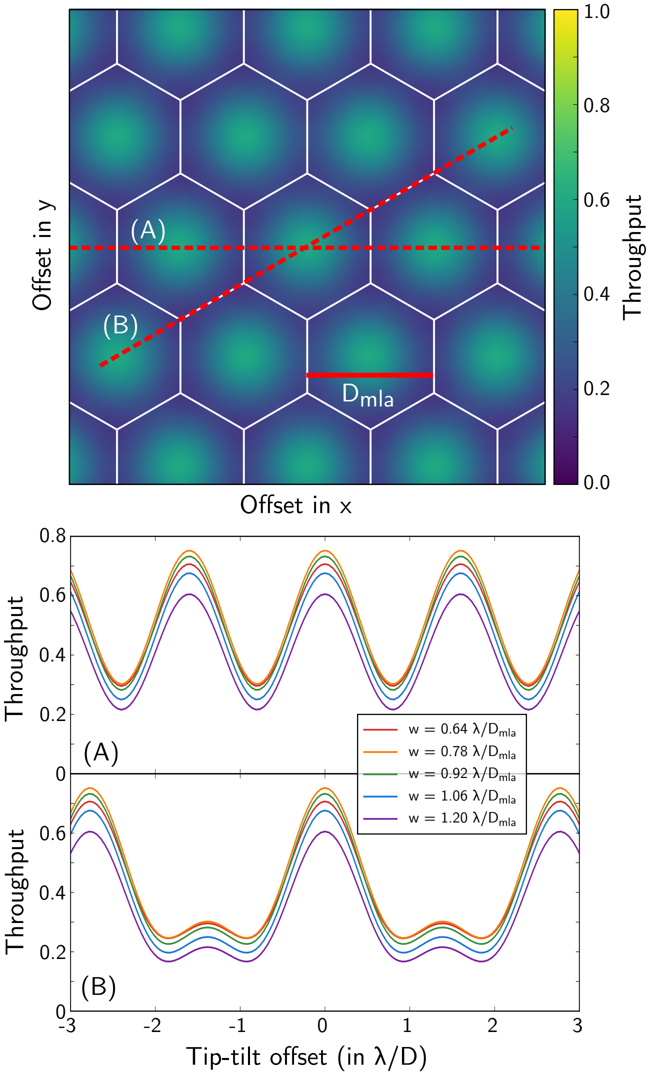

Figure 3.4: Throughput of the single-mode fibers as a function of tip-tilt offset of the source. On the top a two-dimensional throughput map is shown. On the bottom two slices through this map are plotted for several values for the mode field diameter of the single-mode fibers. Maximum throughput of $\sim 72\%$ is reached at the center of a lenslet. On the edge of two microlens the throughput of two fibers have to be added to reach $\sim 30\%$ throughput. The worst case is the triple-point at which the maximum throughput drops to $\sim 25\%$. A fiber mode field radius of $w = 0.78\lambda/D$ achieves the highest throughput for all tip-tilt offsets.

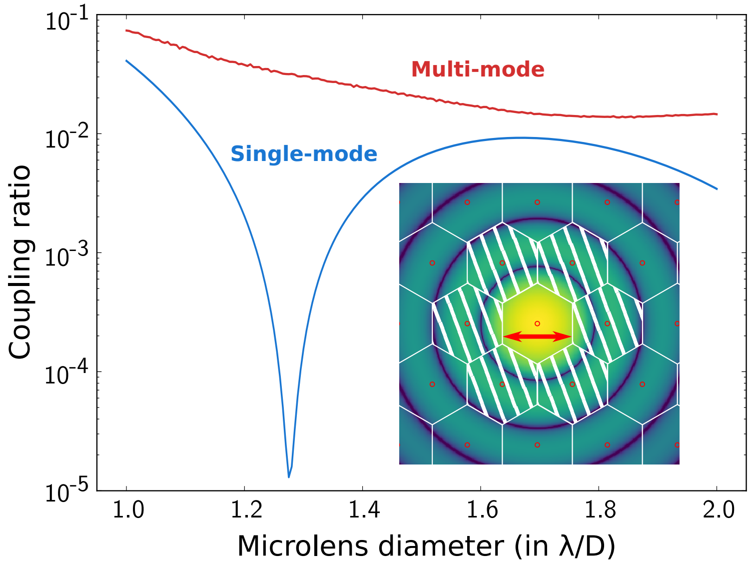

Figure 3.5: Coupling ratio between an on-axis and off-axis source through an off-axis microlens as a function of microlens diameter for a multimode and single-mode fiber. The gain in contrast by using a single-mode fiber can readily be seen in the ratio of these two functions. For most microlens diameters this gain amounts to several orders of magnitude and reaches infinity at $\sim 1.28\lambda/D$ where the light is perfectly nulled on the fiber face by the single-mode fiber. This nulling is first order and is therefore very sensitive to wavelength and centering of the star around the central lenslet.

off-axis fiber is inherently chromatic. We can read off the spectral bandwidth from Fig. 3.5 directly. A contrast of 10^{-4} is reached for $1.26\lambda/D < D_{\mathrm{mla}} < 1.30\lambda/D$, corresponding to a spectral bandwidth of just 3%. Nevertheless this demonstrates that significant gains can be obtained by using single-mode fibers instead of multimode fibers or even conventional intensity detectors.

3.3 Coronagraphy with a single-mode fiber array

3.3.1 Conventional coronagraphy

We can use conventional coronagraphy techniques to reduce the spot intensity and ignore the mode-filtering property in the design process. As an example we use the apodizing phase plate (APP) coronagraph (Codona et al., 2006; Otten et al., 2017; Snik et al., 2012). This coronagraph consists of a single phase-only optic in the pupil plane, making it impervious to tip-tilt vibrations of the telescope or adaptive optics system. The phase pattern is designed to yield a dark zone in a certain region of interest in the focal plane. This region of interest can be both one- and two-sided, and can have arbitrary shapes. Most often the one-sided regions of interest are D-shaped and the two-sided are annular. See Por (2017) for a recent description of APP design. As both the PSF of the star and the planet are altered, the Strehl ratio is maximized to retain planet transmission.

Figure 3.6 shows the contrast through a fiber-fed single-mode fiber array using an APP designed for a contrast of 10^{-5} in a D-shaped region with an inner working angle of $2\lambda/D$ and outer working angle of $10\lambda/D$. While the use of single-mode fibers does enhance the contrast by $\sim 3\times$ on average, this enhancement is not consistent: in some fibers the contrast is enhanced by $> 10\times$ while in others we barely see any improvement at all. This shows that the factor of 3 enhancement that Mawet et al. (2017) finds for a dynamic random speckle field holds true for a single-mode fiber in a static structured speckle field, such as a residual coronagraphic electric field, even when the mode shape is modified from a Gaussian to a constricted Gaussian profile.

3.3.2 Direct pupil-plane phase mask optimization

This improvement brings up the question: can we make use of this mode-filtering in the coronagraph design? As the single-mode fiber array already filters out some electric field modes, the coronagraph does not have to suppress those modes; only modes that are transmitted by the single-mode fiber array need to be suppressed by the coronagraph. The coronagraph needs to minimize the coupling through the single-mode fibers, not the intensity at those positions in the focal plane. Designing a coronagraph specifically for the fiber array therefore allows for more design freedom compared to conventional coronagraph design. In principle, any coronagraph can be designed to take the fiber coupling into account. As a case study, we use a pupil-plane phase plate to alter the PSF in the focal plane. A schematic layout of the proposed system is shown in Fig. 3.1.

To find the phase pattern, we use the novel optimizer from Por (2017), based on the work by Carlotti et al. (2013), that maximizes the throughput (ie. Strehl ratio) for a complex pupil mask, while constraining the stellar intensity in the dark zone to be below the desired contrast. Since the trans-

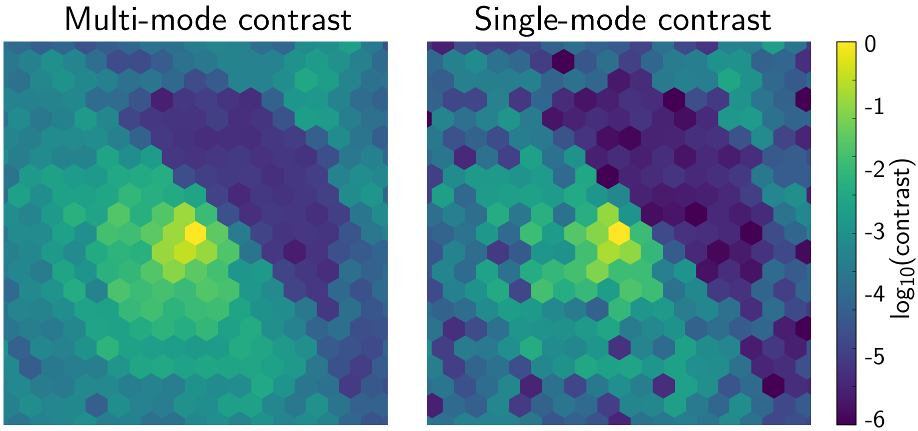

Figure 3.6: Coupling through a microlens array using a conventional APP coronagraph with multimode fibers (left) and single-mode fibers (right). Using a conventional coronagraph such as an APP contrast is still enhanced by the single-mode fibers. The contrast in the dark zone is still enhanced by $\sim 3\times$ on average when using single-mode fibers compared to multimode fibers.

formation between the pupil and focal plane is linear in electric field, this optimization problem is linear, and its global optimum can be easily found using large-scale numerical optimizers such as Gurobi (Gurobi Optimization, 2016). In practice the optimization produces phase-only solutions, which is surprising as non-phase-only solutions are still feasible solutions. As the phase-only optimization problem is simply a more constrained version of the linear one, the phase-only solution must therefore be a global optimum of both problems.

The fiber coupling integral in Eq.3.1, or rather the amplitude of the coupled electric field

$$E_{\text{coupled}} = \frac{\int E_{\text{in}}^{*} E_{\text{sm}} \mathrm{d}A}{\left| \int E_{\text{sm}} \mathrm{d}A \right|} \tag{3.5}$$

is still linear in the input electric field E_{in}, so we can apply the same method here. We maximize the throughput of the central fiber, while constraining the coupling through the specified off-axis fibers. To counter the chromaticity mentioned in Sect. 3.2.2, we constrain the off-axis stellar intensity at several wavelengths simultaneously, which ensures that the contrast is attained over a broad spectral bandwidth. Jitter resistance is kept in check in a similar manner: the desired raw contrast must be attained for several

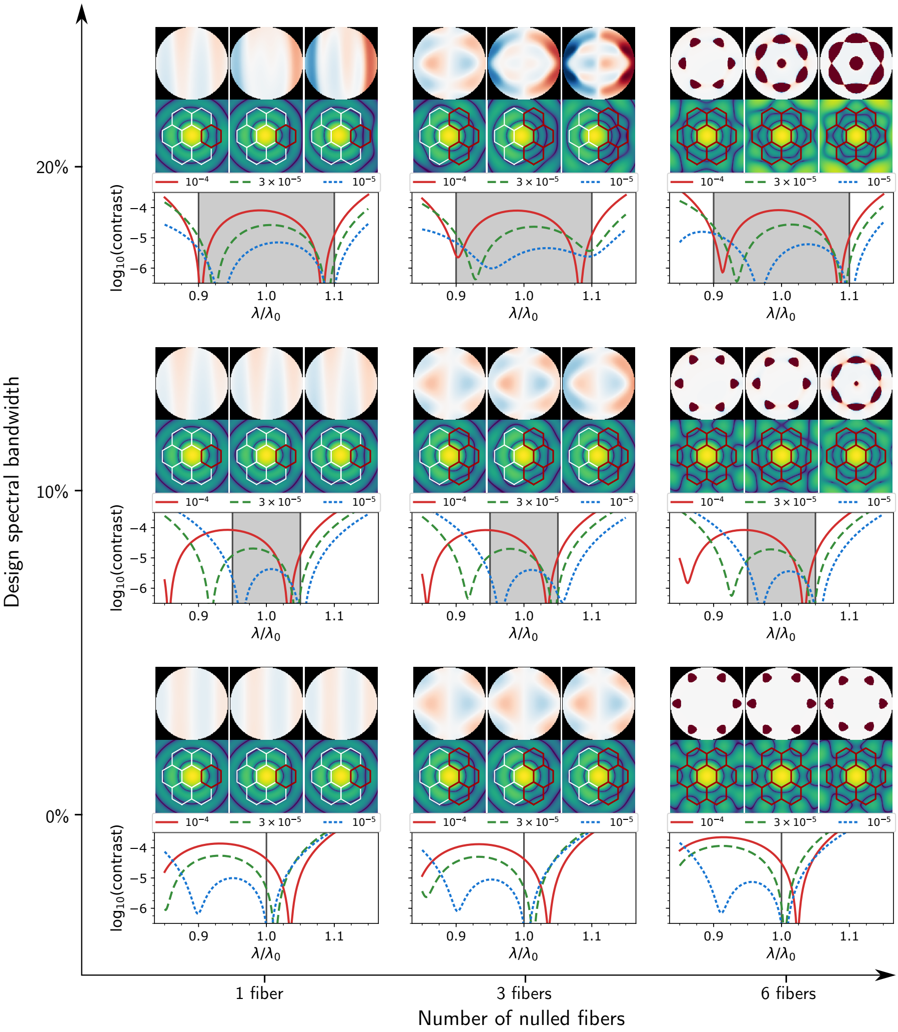

Figure 3.7: A series of optimizations for one, three and six fibers on the first ring of microlenses for a clear aperture. The design spectral bandwidth were 0%, 10% and 20% and the contrasts 1×10^{-4}, 3×10^{-5} and 1×10^{-5}. A $0.06\lambda/D$ peak-to-peak telescope tip-tilt jitter was also taken into account. Each microlens has a circum-diameter of $1.8\lambda/D$. For each SCAR design we show the pupil-plane phase pattern, its corresponding point spread function and its raw contrast η_s/η_p as a function of wavelength averaged over the marked fibers. The chromatic response shows the raw contrast after the single-mode fiber. The second-order nulling on the fiber face is clearly visible in every design. In Table 3.1 we list the fixed and varied parameter in this figure. The throughput of all SCAR designs shown in this figure can be found in Figure 3.9.

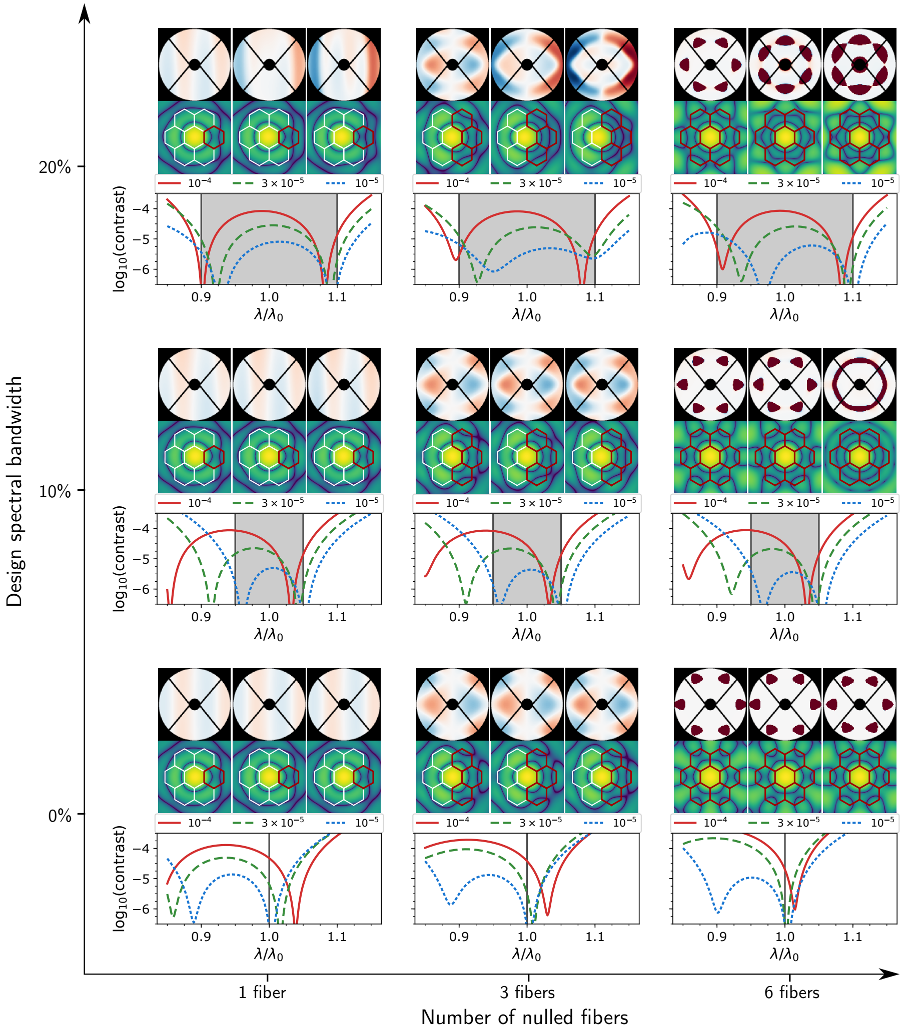

Figure 3.8: The same as Fig. 3.7 for a VLT aperture. The aperture was subject to a 1% binary erosion, ie. undersizing the pupil and oversizing central obscuration, spiders and other pupil features by 1% of the aperture size, to accommodate a pupil misalignment. The general structure of the solutions is similar to the case of a clear aperture. The central obscuration increases the strength of the first Airy ring, thereby decreasing the throughput of these SCAR designs slightly. The relatively thin spiders have no influence on the throughput at these angular separations. In Table 3.1 we list the fixed and varied parameter in this figure. A summary of the throughput of all SCAR designs shown in this figure can be found in Fig. 3.9.

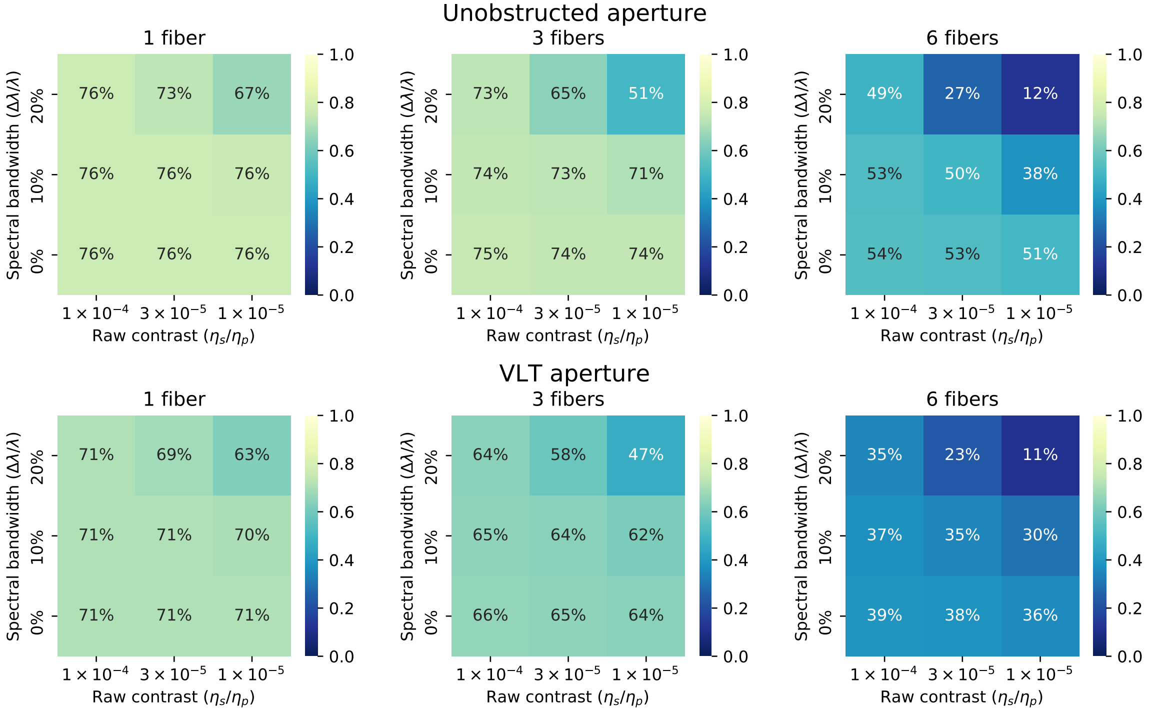

Figure 3.9: The throughput (η_p) for the SCAR designs shown Figs. 3.7 and 3.8. The shown throughput is the total throughput of the coronagraphic system. It includes the Strehl reduction of the phase plate, the spatial filtering of the microlenses and the mode filtering of the single-mode fibers. This throughput is achieved through a single single-mode fiber when the planet is located directly on top of an off-axis lenslet. The throughput at other positions varies generally according to Figure 3.4, but varies slightly depending on the specific SCAR design.

Table 3.1: The design parameters used for all SCAR designs throughout this work. All SCAR designs generated with these parameters can be found in Figures 3.7 and 3.8.

Parameter name	Value
Raw contrast limit	$\{1 \times 10^{-4}, 3 \times 10^{-5}, 1 \times 10^{-5}\}$
Spectral bandwidths	$\{0\%, 10\%, 20\%\}$
Tip-tilt errors	$0.06\lambda/D$ peak-to-peak
Microlens circum-diameter	$1.8\lambda/D$
Microlens shape	Hexagonal
Fiber mode shape	Gaussian
Fiber mode field diameter	$1.7\lambda/D_{\mathrm{mla}}$
Pupil mask	$\{\mathrm{unobstructed}, \mathrm{VLT}\}$

tip-tilt positions simultaneously.

In Fig. 3.7 we show a few examples of optimizations for one, three and six fibers for a contrast of 1×10^{-4}, 3×10^{-5} and 1×10^{-5} using a $0\%, 10\%$ and 20% spectral bandwidth, along with their corresponding PSF and chromatic response. The design parameters are shown in Table 3.1. These design parameters were chosen to show a variety of SCAR designs for realistic implementations. At the shown contrast limits, the residual atmospheric speckles will limited the on-sky contrast, even after an extreme AO system. The spectral bandwidths were chosen as wide as possible, without compromising on planet throughput. The resulting spectral bandwidths are large enough to apply spectral cross-correlation techniques.

In each case the optimizer prefers a second order null. This second order null is much more stable against bandwidth and tip-tilt jitter. The reason for this is explained graphically in Fig. 3.2. Furthermore, this second order null is even present in monochromatic optimizations and in optimizations without accommodation for tip-tilt errors. This means that the second-order null requires less phase stroke to achieve and therefore provides higher Strehl ratios.

As the optimizer can handle arbitrary apertures, optimizations for other aperture shapes are also possible. Figure 3.8 shows optimizations for a VLT aperture for the same parameters as for the clear apertures. The aperture was subject to a 1% binary erosion, ie. undersizing the pupil and oversizing central obscuration, spiders and other pupil features by 1% of the aperture size, to accommodate for a misalignment in the pupil mask. Although the overall structure is quite similar, there is one key difference compared to

Table 3.2: The different throughput terms that are important for the SCAR coronagraph. A distinction is made between theoretical and experimental terms. Experimental throughput terms will be non-existent with perfect manufacturing, while theoretical throughput terms are unavoidable. Typical values in the visible are shown for each term. The values for the experimental throughput terms are indicative of current technology performance and may increase as technology matures.

Throughput term	Typical values
Theoretical	
Geometric lenslet throughput	$\sim 80\%$
Fiber injection losses	$90\% - 95\%$
Planet location	$50\% - 100\%$
Phase plate Strehl reduction	$60\% - 80\%$
Total	$\sim 41\%$
Experimental	
Phase plate transmission	$> 85\%$
Fresnel losses on the fiber	$\sim 90\%$
Microlens transmission	$> 95\%$
Strehl ratio of the AO system	$\sim 50\%$
Total	36%
Total	14%

a clear aperture: the relative transmission T is lower for all phase plate designs. This means that the relative transmission depends strongly on the size of the central obscuration. This is obvious as larger central obscurations strengthen the first Airy ring and brighter features typically cost more stroke, and therefore relative transmission, to change, similar to conventional APP design. Effectively, this means that each feature in the phase pattern becomes larger to compensate for larger central obscurations.

We summarize the multitude of SCAR phase pattern designs in Figure 3.9. This figure shows the total planet throughput η_p, provided that the planet is located in the center of the off-axis microlens. This throughput includes all theoretically unavoidable terms, but excludes all experimental terms. A summary of important throughput terms are listed in Table 3.2.

In the rest of this paper, we consider the outlined SCAR design in Fig. 3.7 and 3.8 using a 10% spectral bandwidth for a contrast of 3×10^{-5}. Although optimized for only 10%, this specific design performs exceptionally well and a contrast of $< 10^{-4}$ is obtained for a spectral bandwidth of

18% centered around the design wavelength.

3.4 Single-mode fiber coronagraph properties

In this section we show the properties of this new coronagraph and perform parameter studies on the fixed parameters in Table 3.1. We discuss the mode field diameter of the single-mode fiber in Sect. 3.4.1, throughput and inner working angle in Sect. 3.4.2, the chromatic response in Sect. 3.4.3, the tip-tilt sensitivity of the SCAR designs in Sect. 3.4.4 and the sensitivity of other modes in Sect. 3.4.5.

3.4.1 Fiber mode field diameter

The phase plate reduces the throughput of planet light. This reduction will also affect the optimal value of the mode field diameter. Smaller mode field diameters result in larger back-propagated fiber modes in the focal plane, which makes it easier to squeeze the three rings necessary for the second-order nulling into this mode. Therefore, we expect higher Strehl ratios (the throughput relative to the unaltered PSF throughput) as the mode field diameter becomes smaller. This is superimposed on the actual throughput of the unaltered PSF. Both curves are shown in Fig. 3.10 for both a clear and the VLT aperture.

3.4.2 Throughput and inner working angle

The throughput shown here is the fractional transmission of light from the entire pupil into the central single-mode fiber: it includes all theoretical terms as listed in Table 3.1. It however excludes all experimental terms. It is clear that larger microlenses generally give a better throughput, as is expected. Additionally, we can see that the optimal mode field diameter as a function of microlens diameter for the unaltered PSF moves to larger mode field diameters, as it is essentially matching the Airy-core width rather than the size of the microlens itself. The optimal mode field diameter for the SCAR however stay the same as smaller mode field diameter have an advantage in their Strehl ratio.

Figure 3.11 shows the throughput (η_p) of the coronagraph for different values for the microlens diameter. The mode field radius of the fiber was fixed at $w = 0.85\lambda/D_{\mathrm{mla}}$ and the contrast at 3×10^{-5}. We adopted a $0.1\lambda/D$ rms telescope tip-tilt jitter with a normal distribution, corresponding to a 2 mas rms tip-tilt jitter at a wavelength of $\lambda = 750$nm. This level of tip-tilt

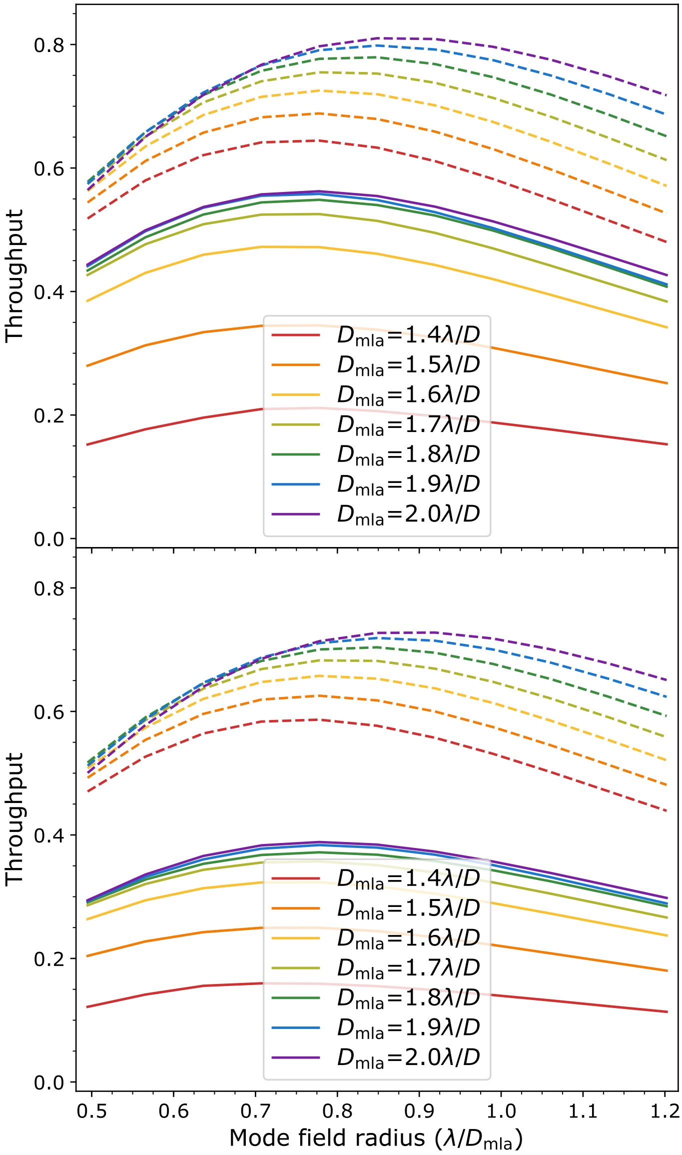

Figure 3.10: Throughput of the central lenslet as a function of mode field radius for various values of the microlens diameter. Each data point represents a different SCAR design. Solid lines indicate the SCAR PSFs, dashed lines an unaltered PSF. The top panel shows the throughput for an clear aperture, the bottom panel for a VLT aperture.

jitter was chosen to mimic a SPHERE-like adaptive optics system, according to Fusco et al. (2016). The throughput is averaged over all pointing positions and over the full 10% spectral bandwidth. The throughput of off-center fibers is negligible to that of the central fiber: all throughput is concentrated in only one single-mode fiber.

As the stellar throughput is only minimized for the first ring of microlenses, we do not have much throughput beyond the edge of the first off-axis microlens. Designs can be made for more than one ring of microlenses, although this complicates the design procedure and will be discussed in future work. Extremely close to the star, we have no throughput, as the Airy core is still mostly on the central lenslet. At $\sim 0.5\lambda/D$ the throughput starts to rise, reaching a maximum at the center of the first microlens. A throughput of $\sim 50\%$ of the maximum SCAR throughput is already reached at $\sim 1\lambda/D$, which is the usual definition of inner working angle. Also, up to microlens diameters of $\sim 1.8\lambda/D$ the throughput at small angular separations ($< 1\lambda/D$) does not change much, but the maximum throughput still increases. For larger microlens diameter we still gain in throughput at the center of the microlens, however the throughput at these small angular separations starts to suffer, which is especially visible in the $D_{\mathrm{mla}} = 2.0\lambda/D$ throughput curve.

Lines for the theoretical throughput of other coronagraphs are overplotted in Fig. 3.11. Perfect coronagraphs refer to the notion introduced by Cavarroc et al. (2006) and Guyon et al. (2006). A second-order perfect coronagraph removes a constant term from the pupil-plane electric field. A fourth-order additionally removes the x and y components from the electric field. A sixth-order perfect coronagraph furthermore removes the x^2, xy and y^2 modes from the electric field. For the theoretical coronagraphs, the throughput is calculated using a circular aperture of $0.7\lambda/D$ centered around the off-axis planet. We can see that the SCAR throughput lags behind the theoretical second-order coronagraph, but stays close to the fourth-order and beats the sixth-order at angular separations $< 1.7\lambda/D$.

Figure 3.12 shows the relative integration time (η_s/η_p^2) under the same conditions as in Fig. 3.11. We now see that, even though the throughput of the theoretical second-order coronagraph is good, its integration time is minor because it does not outweigh the loss in starlight suppression. SCAR however performs similar to theoretical fourth-order coronagraph for angular separations $< 1.8\lambda/D$. A sixth-order coronagraphs does even better, but suffers from a lack of throughput which becomes noticeable in cases where the raw contrast (η_s/η_p) is limited, which is the case in any

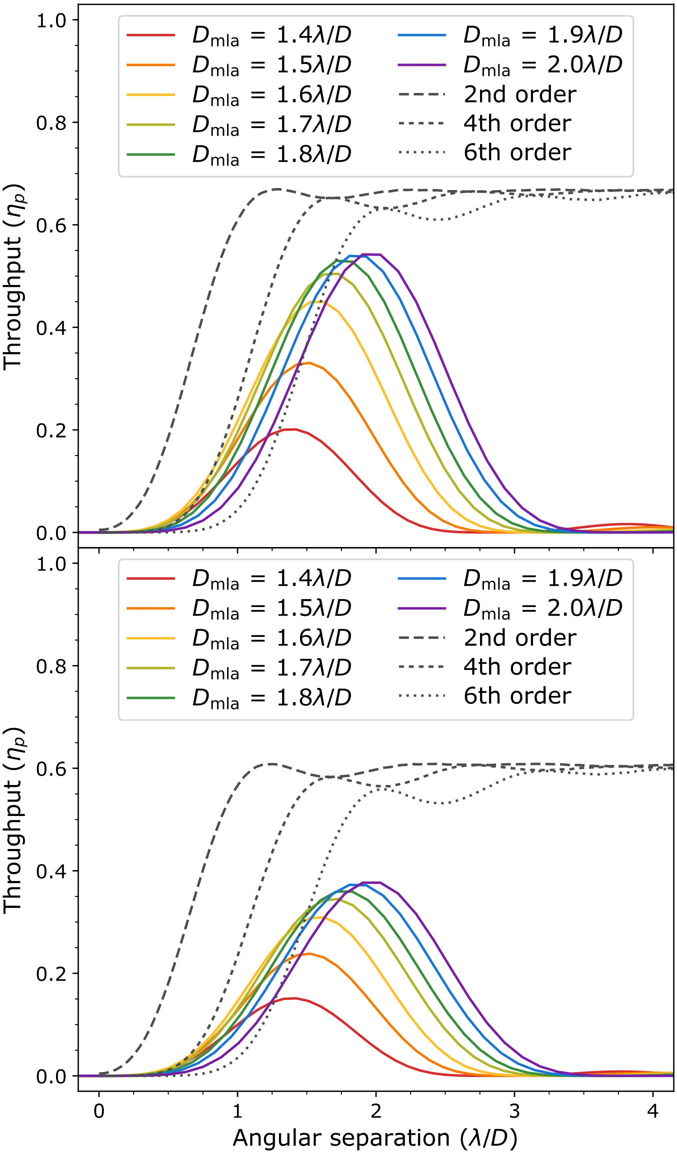

Figure 3.11: Throughput as function of off-axis angle for various values of the microlens diameter. The throughput of a perfect second, fourth and sixth-order coronagraph is also plotted. The top panel shows the throughput for an unobstructed aperture, the bottom panel for the VLT aperture. The throughput is calculated for the optimal position angle of the off-axis source (ie. directly across an off-axis microlens). The throughput for the theoretical coronagraphs is taken to be the fractional flux within an aperture of radius $0.7\lambda/D$ centered around the planet.

ground-based telescope. This suggests that SCAR is a close-to-optimal coronagraph.

3.4.3 Spectral bandwidth

Figures 3.7 and 3.8 show the chromatic response for all designs. Every design exhibits the double-dipped structure of the second-order null on the fiber. For all designs with a non-zero spectral bandwidth, we can also see that the contrast is hard to achieve on the long wavelength side. At these longer wavelengths the bright Airy core starts to grow into the microlens array. This means that the second Airy ring needs to be made much brighter to compensate, which requires substantial deviations in the phase pattern. Qualitatively, the location of the second null is chosen by the optimizer such that the spectral bandwidth requirement is reached.

3.4.4 Tip-tilt sensitivity and stellar diameter

Figure 3.13 shows the average contrast (η_s/η_p) over the full 10% bandwidth as a function of tip-tilt error upstream of the fiber injection unit. The double-dip structure is again clearly visible, which greatly improves the tip-tilt response. Both coronagraph designs achieve a tip-tilt stability of $\sim 0.1\lambda/D$ rms. This figure also shows that the SCAR coronagraph is insensitive for stars with an angular diameter up to $0.1\lambda/D$.

3.4.5 Sensitivity to other aberrations

To show the sensitivity to other aberrations, we perform a sensitivity analysis on the SCAR coronagraph: we aim to find the mode basis of orthogonal modes ordered by their sensitivity. These principal modes can be found by taking the first-order Taylor expansion of the phase in the pupil-plane around the nominal position. In this way a linear transformation G_λ can be constructed from a phase deformation $\delta\varphi$ to the resulting change in electric field in the fibers δE_λ:

$$\delta E_\lambda = G_\lambda \delta\varphi. \tag{3.6}$$

G_λ and δE_λ both depend on wavelength as the response of the coronagraph is inherently chromatic. A singular value decomposition of the matrix G_λ yields the monochromatic principal phase modes of the coronagraph. The corresponding singular values denote the importance of those modes. This expansion is similar to the one used in electric field conjugation (Give'on et al., 2007).

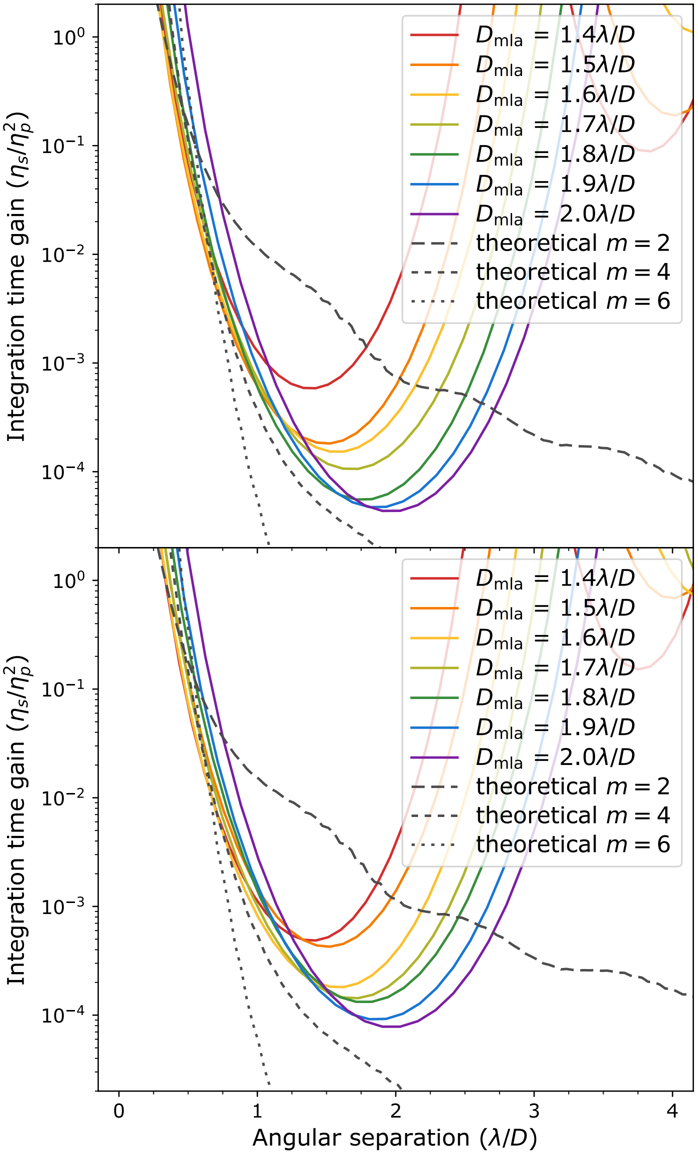

Figure 3.12: Relative integration time (η_s/η_p^2) as function of off-axis angle for various values of the microlens diameter. The top panel shows the relative integration time for an unobstructed aperture, the bottom panel for the VLT aperture. The integration time for the theoretical coronagraphs is calculated on the flux within an aperture of radius $0.7\lambda/D$ centered around the planet.

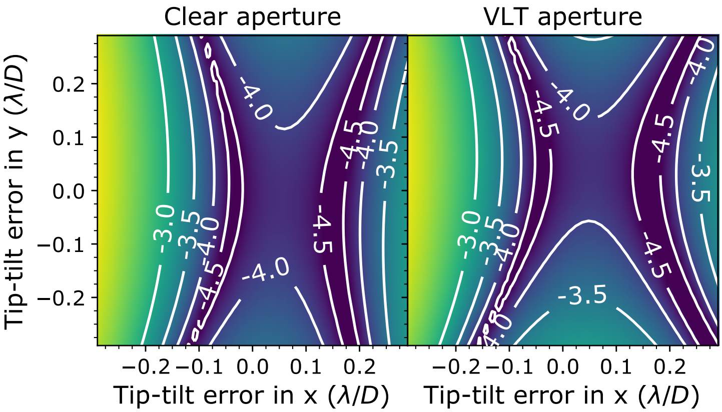

Figure 3.13: Map of the worst contrast through an off-axis fiber over a 10% bandwidth as a function of tip-tilt error upstream of the microlens array. This shows that the coronagraph is reasonably stable against tip-tilt, allowing for a $\sim 0.15\lambda/D$ tip-tilt error until the contrast drops to 10^{-4}. The contour labels indicate $\log_{10}(\eta_s/\eta_p)$.

Broadband principal modes can be obtained by stacking several G_λ matrices for wavelengths within the spectral bandwidth into a single matrix G as

$$\begin{bmatrix} \delta E_{\lambda_1} \\ \delta E_{\lambda_2} \\ \vdots \\ \delta E_{\lambda_N} \end{bmatrix} = \begin{bmatrix} G_{\lambda_1} \\ G_{\lambda_2} \\ \vdots \\ G_{\lambda_N} \end{bmatrix} \delta\varphi. \tag{3.7}$$

A singular value decomposition on the matrix G now yields the broadband principal modes. The singular values are now indicative of the amount of electric field each phase mode induces in the fibers as a function of wavelength. This method is again similar to the one used in broadband electric field conjugation (Give'on et al., 2007).

Figure 3.14 shows the broadband principal modes for the SCAR design for the VLT aperture, along with their singular values. Only six modes are important for the final contrast. Naively we would expect two modes per fiber, so 12 modes in total, as we need to control both the real and imaginary part of the electric field. However in our case the system shows an antihermitian symmetry: the transmitted electric field on fibers in opposite points in the focal plane are not independent if only small phase aberrations are present. This means that one phase mode determines the electric field for both fibers so that only two modes per two fibers are needed. Only half of the original 12 modes determine the contrast in a monochromatic system, meaning that six modes are left. The omitted six modes correspond to amplitude errors. For the broadband principal modes we of course expect some additional modes with low importance, corresponding to the spectral bandwidth increase. The first six of these are shown as modes 7 to 12 in Fig. 3.14.

The first principal mode is trefoil, which is the result of the six-fold symmetry in the fiber locations. The second trefoil is missing: its corresponding electric field change is completely filtered out by the single-mode fibers: it creates radial first-order nulls directly on the center of every lenslet. Other important modes include secondary-astigmatism-like modes for modes 2 and 3, coma-like modes for modes 4 and 5, and a perturbed spherical mode for mode 6.

In Fig. 3.15 we show the response of the SCAR coronagraph to each of these modes. The average normalized irradiance is the average raw contrast over the full spectral bandwidth and all six fibers in the first ring of microlenses. It can be seen that the response for the first six modes is generally a lot stronger than that of the last six. The average raw contrast is limited by the residual leakage from the SCAR coronagraph at the low aberration end, while the contrast increases when more aberration is added. Additionally, we can see different behaviour, depending on the mode that we are looking at. Some modes (modes 1 to 6, 9, 11 and 12) show quadratic behaviour, while others (modes 7, 8 and 10) show a fourth order behaviour. Also notice that mode 7 actually increase the average raw contrast. While this may seem an impossibility, as the SCAR coronagraph is optimized for raw contrast, in these cases the fibers on one side become brighter than the contrast constraint, while the others compensate by becoming dimmer. This would actually decrease the effectiveness of the coronagraph while still increasing the average raw contrast.

3.5 Comparison to the vortex coronagraph

The described performance of the SCAR coronagraph begs the question on how it compares to other coronagraphs using single-mode fibers. In this section we will provide a comparison of the SCAR coronagraph with the single-mode fiber injection unit with vortex coronagraph proposed by Mawet et al. (2017), and a comparison with a multiplexed fiber injection unit as shown in Sect. 5.5 behind a vortex coronagraph. Figure 3.16 shows

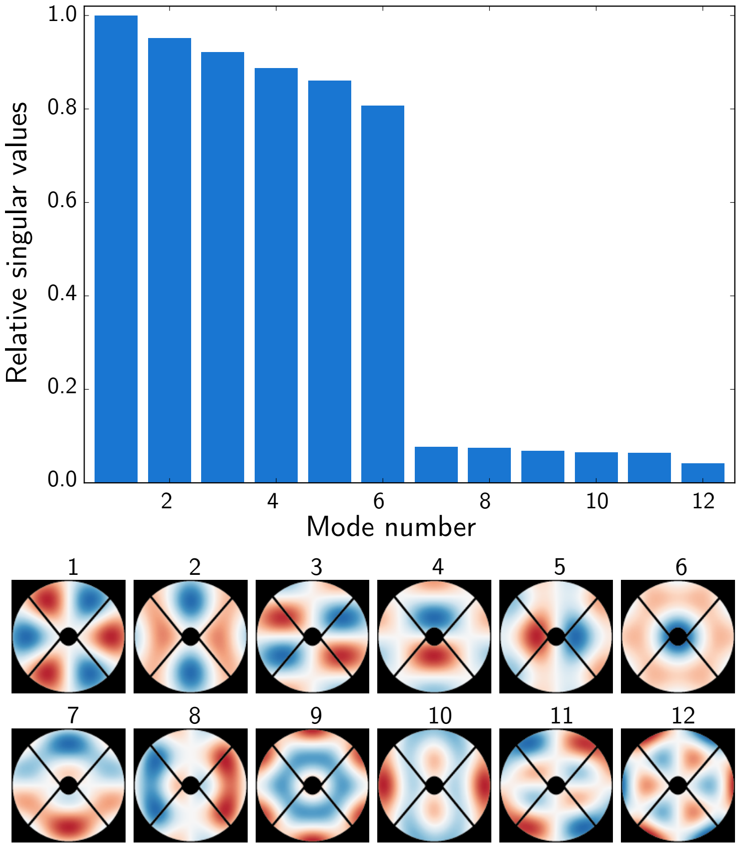

Figure 3.14: Principal phase modes for the SCAR coronagraph using the design described in the text. The top panel shows the singular value of each mode, indicating its significance for the obtained contrast after phase correction. The bottom panel shows the pupil-plane phase for each mode.

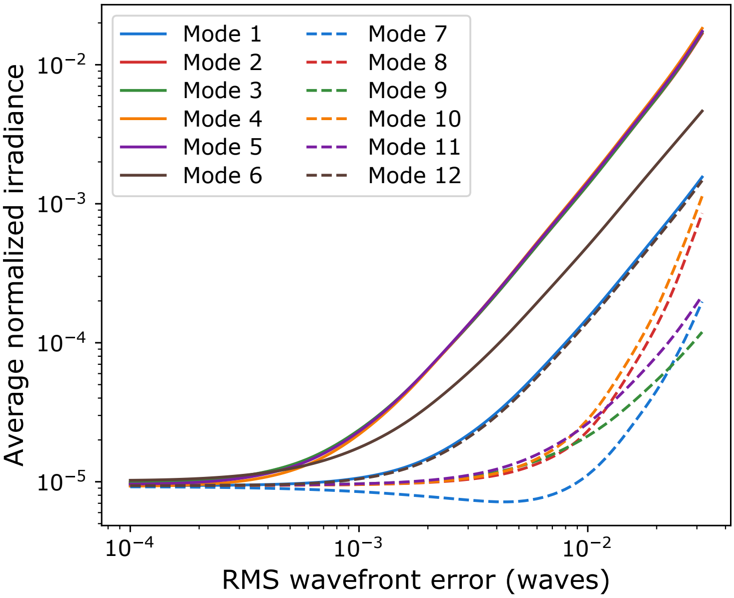

Figure 3.15: Average normalized irradiance for each of the modes in Fig. 3.14. The normalized irradiance is averaged over all fibers in the first ring of microlenses, and over the full 10% spectral bandwidth. These curves can yield constraints on the post-AO residual variance for each of the shown modes. Higher-order modes in this expansion generally have less response and do not have to be controller as well as low-order modes.

the throughput and relative integration time of a conventional vortex coronagraph using a clear aperture. A conventional intensity detector (ie. sum of all flux in an aperture centered around the star) is compared with a single-mode fiber centered around the planet. The mode field diameter was optimized for maximum throughput of the PSF without a coronagraph. To better capture the best and worst case performance for comparison with the vortex coronagraph, we take a telescope tip-tilt jitters of $0.05\lambda/D$ for the best case performance and $0.15\lambda/D$ for the worst case performance Similarly to Fig. 3.11, a telescope tip-tilt jitter of $0.1\lambda/D$ rms was chosen.

For charges $m = 4$ and $m = 6$ a decrease in throughput, compared to the vortex coronagraph with multimode fiber, can be seen, approximately corresponding with the maximum coupling of an Airy pattern through a Gaussian single-mode fiber. Additionally the vortex in the focal plane imprints a phase ramp on off-axis sources, which degrades throughput even further. This effect is more pronounced with smaller angular separations and higher charge vortices. Most of this phase ramp can be easily negated by tilting the fiber slightly, depending on the focal-plane position of the planet. We can see that the SCAR coronagraph wins in throughput compared to vortex coronagraphs with charger $m > 2$. However the charge 2 vortex coronagraph does not suppress the star very well, resulting in a moderate relative integration time compared to the SCAR coronagraph.

Figure 3.17 shows the throughput and relative integration time of a vortex coronagraph charge $m = 2$ through a microlens-fed single-mode fiber-array as the fiber injection unit. The diameter of the microlenses is varied from 1.4 to $2.0\lambda/D$, and the mode field diameter is optimized for maximum throughput of an Airy pattern. For large angular separations the throughput oscillates due to the transmission of the microlens array as shown in Fig. 3.4. For the first ring of microlenses the throughput rises quickly, again reaching its maximum at the center of the microlens. Even though the coupling efficiency for smaller microlenses is higher, the geometric throughput decreases more rapidly. A trade-off between these two throughput terms leads to an optimal microlens diameter of $\sim 1.8\lambda/D$ for the vortex coronagraph as well. The throughput at this microlens diameter is comparable to the performance of the SCAR coronagraph even though the vortex coronagraph has a more complicated optical setup. This multiplexed single-mode fiber vortex coronagraph however does not suppress starlight as well as the SCAR, leading to a worse relative integration time. The vortex coronagraph however does have the advantage of an infinite outer working angle.

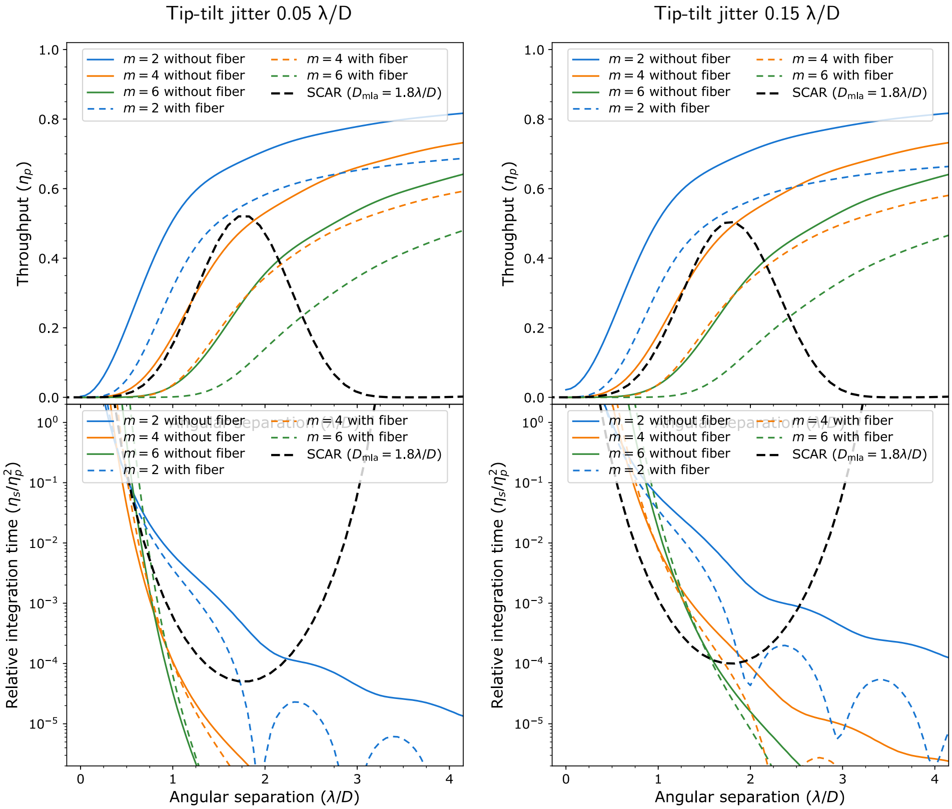

Figure 3.16: The throughput (η_p) and relative integration time (η_s/η_p^2) for a vortex coronagraph using a clear aperture for charges $m = 2, 4, 6$ using a conventional intensity detector or a single-mode fiber centered around the planet. A telescope tip-tilt jitter of (left column) $0.05\lambda/D$ or (right column) $0.15\lambda/D$ rms was taken into account. These values correspond to a best and worst case performance of the adaptive optics system. The throughput is calculated for the optimal position angle of the off-axis source (ie. directly across an off-axis microlens). For the vortex coronagraph without fiber, the throughput and relative integration time is calculated on an aperture of radius $0.7\lambda/D$ centered around the planet.

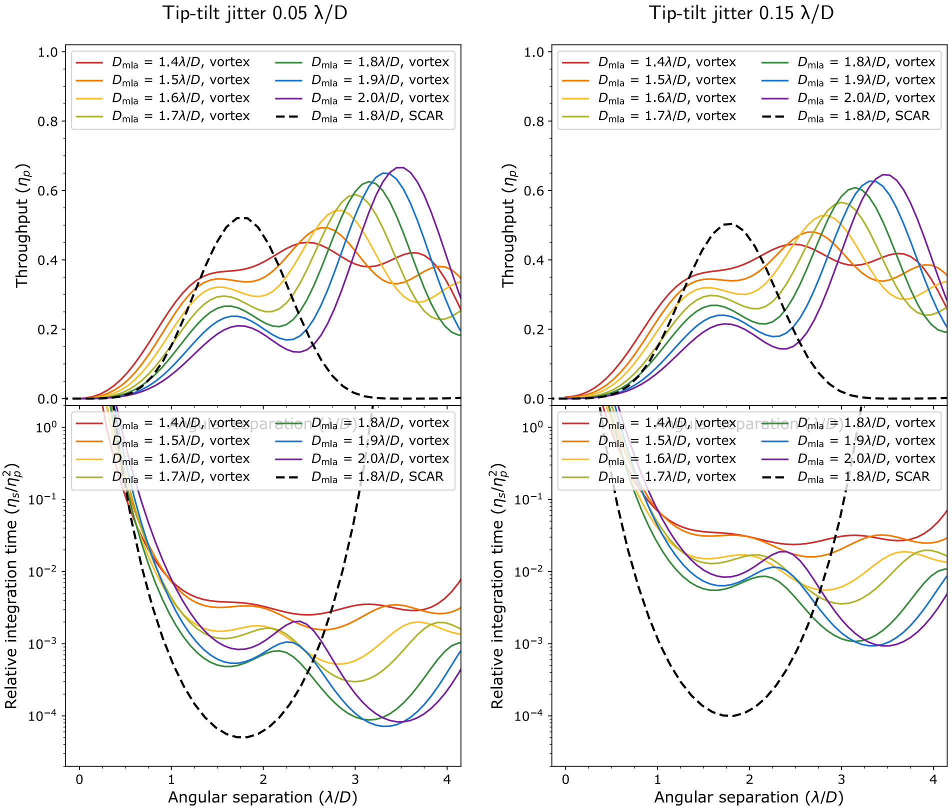

Figure 3.17: The throughput (η_p) and relative integration time (η_s/η_p^2) of a charge $m = 2$ vortex coronagraph on a microlens-fed single-mode fiber array. The diameter of the microlenses is varied from 1.4 to $2.0\lambda/D$, and the mode field diameter is optimized for maximum throughput of an Airy pattern. The throughput of the SCAR coronagraph designed for $1.8\lambda/D$ microlens diameter was added for comparison. The assumed tip-tilt jitter is (left column) $0.05\lambda/D$ or (right column) $0.15\lambda/D$ rms. These values correspond to a best and worst case performance of the adaptive optics system. The throughput is calculated for the optimal position angle of the off-axis source (ie. directly across an off-axis microlens).

3.6 Conclusion

In this paper we described the principle behind coronagraphs leveraging the design freedom offered by the use of single-mode fibers as a mode filter. We have shown the properties of a microlens-array fed single-mode fiber-array, making it possible to perform exoplanet searches. We combined this with a pupil-plane phase plate, yielding the SCAR coronagraph and presented the following advantages of this new coronagraph:

1. *Low inner working angles.* Inner working angles as low as $1\lambda/D$ can be reached using current designs.
2. *High throughput.* These designs reach a maximum throughput of 50% and 30% for a clear and the VLT aperture, respectively.
3. *High contrast.* Starlight can be suppressed to $< 3 \times 10^{-5}$ for the six fibers surrounding the star over the full spectral bandwidth until the throughput starts to drop.
4. *Broad spectral bandwidth.* This suppression is achieved over the full 20% spectral bandwidth.
5. *Robust against tip-tilt errors.* The SCAR coronagraph is stable against $\sim 0.1\lambda/D$ rms tip-tilt errors upstream due to the use of second order nulling on the fibers.
6. *Residual speckle suppression.* Residual speckles are are reduced by $\sim 3\times$ in intensity, due to the coupling efficiency of a random electric field into the single-mode fibers.

All advantages can be obtained into a single SCAR design. All these advantages make this coronagraph a prime candidate for future upgrades of extreme AO systems. In particular, the SCAR coronagraph is perfectly suited for spectral characterization of Proxima b: it satisfies all coronagraphic requirements set by Lovis et al. (2017). A companion paper (Haffert et al., 2018) provides a tolerancing study for this specific application.

Future research will explore active control of the fiber throughput of the SCAR coronagraph. Application of the SCAR methodology to other coronagraphs is also left for future research. An interesting example in this case is the design of a Lyot-plane mask for a conventional Lyot or vortex coronagraph, akin to Ruane et al. (2015a). Even optimizing the focal-plane mask itself might be realizable for the fiber array in these coronagraphs (Ruane et al., 2015b).

Another avenue is the use of photonic technologies to further process the light in the fibers. A simple example is the use of fiber Bragg gratings for filtering the atmospheric OH lines (Trinh et al., 2013). Another example is building a phase-shifting interferometer of the six fibers. This will provide information about the coherence of the light in each of the fibers with respect to the star, and would allow for synchronous interferometric speckle subtraction (Guyon, 2004).

References

Aime, C., & Soummer, R. 2004, The Astrophysical Journal Letters, 612, L85

Anglada-Escudé, G., Amado, P. J., Barnes, J., et al. 2016, Nature, 536, 437

Beuzit, J.-L., Feldt, M., Dohlen, K., et al. 2008, in SPIE Astronomical Telescopes+ Instrumentation, International Society for Optics and Photonics, 701418–701418

Borucki, W. J., Koch, D. G., Basri, G., et al. 2011, The Astrophysical Journal, 736, 19

Brogi, M., Snellen, I. A., de Kok, R. J., et al. 2012, Nature, 486, 502

Carlotti, A., Kasdin, N. J., Vanderbei, R. J., & Riggs, A. E. 2013, in SPIE Optical Engineering+ Applications, International Society for Optics and Photonics, 88641Q–88641Q

Cavarroc, C., Boccaletti, A., Baudoz, P., Fusco, T., & Rouan, D. 2006, Astronomy & Astrophysics, 447, 397

Codona, J., Kenworthy, M., Hinz, P., Angel, J., & Woolf, N. 2006, in SPIE Astronomical Telescopes+ Instrumentation, International Society for Optics and Photonics, 62691N–62691N

Corbett, J. C. 2009, Optics express, 17, 1885

Fusco, T., Sauvage, J.-F., Mouillet, D., et al. 2016, in SPIE Astronomical Telescopes+ Instrumentation, International Society for Optics and Photonics, 99090U–99090U

Give'on, A., Kern, B., Shaklan, S., Moody, D. C., & Pueyo, L. 2007, in Optical Engineering+ Applications, International Society for Optics and Photonics, 66910A–66910A

Gurobi Optimization, I. 2016, Gurobi Optimizer Reference Manual. `http://www.gurobi.com`

Guyon, O. 2004, The Astrophysical Journal, 615, 562

—. 2005, The Astrophysical Journal, 629, 592

Guyon, O., Pluzhnik, E., Kuchner, M., Collins, B., & Ridgway, S. 2006, The Astrophysical Journal Supplement Series, 167, 81

Haffert, S. Y., Por, E. H., Keller, C. U., et al. 2018, arXiv e-prints, arXiv:1803.10693. `https://arxiv.org/abs/1803.10693`

Haguenauer, P., & Serabyn, E. 2006, Applied optics, 45, 2749

Hanot, C., Mennesson, B., Martin, S., et al. 2011, The Astrophysical Journal, 729, 110

Jovanovic, N., Martinache, F., Guyon, O., et al. 2015, Publications of the Astronomical Society of the Pacific, 127, 890

Kawahara, H., Murakami, N., Matsuo, T., & Kotani, T. 2014, The Astrophysical Journal Supplement Series, 212, 27

Kipping, D. M., Cameron, C., Hartman, J. D., et al. 2017, The Astronomical Journal, 153, 93

Konopacky, Q. M., Barman, T. S., Macintosh, B. A., & Marois, C. 2013, Science, 339, 1398

Lovis, C., Snellen, I., Mouillet, D., et al. 2017, Astronomy & Astrophysics, 599, A16

Macintosh, B., Graham, J. R., Ingraham, P., et al. 2014, Proceedings of the National Academy of Sciences, 111, 12661

Marcuse, D. 1978, JOSA, 68, 103

Marois, C., Lafreniere, D., Doyon, R., Macintosh, B., & Nadeau, D. 2006, The Astrophysical Journal, 641, 556

Martin, S., Serabyn, E., Liewer, K., et al. 2008, in Proc. SPIE, Vol. 7013. `https://doi.org/10.1117/12.789484`

Mawet, D., Pueyo, L., Lawson, P., et al. 2012, in SPIE Astronomical Telescopes+ Instrumentation, International Society for Optics and Photonics, 844204–844204

Mawet, D., Ruane, G., Xuan, W., et al. 2017, The Astrophysical Journal, 838, 92

Otten, G. P., Snik, F., Kenworthy, M. A., et al. 2017, The Astrophysical Journal, 834, 175

Pepe, F. A., Cristiani, S., Lopez, R. R., et al. 2010, in SPIE Astronomical Telescopes+ Instrumentation, International Society for Optics and Photonics, 77350F–77350F

Por, E. H. 2017, in Techniques and Instrumentation for Detection of Exoplanets VIII, Vol. 10400, International Society for Optics and Photonics, 104000V

Riaud, P., & Schneider, J. 2007, Astronomy & Astrophysics, 469, 355

Ruane, G. J., Huby, E., Absil, O., et al. 2015a, Astronomy & Astrophysics, 583, A81

Ruane, G. J., Swartzlander, G. A., Slussarenko, S., Marrucci, L., & Dennis, M. R. 2015b, Optica, 2, 147

Snellen, I., de Kok, R., Birkby, J., et al. 2015, Astronomy & Astrophysics, 576, A59

Snellen, I. A., Brandl, B. R., de Kok, R. J., et al. 2014, Nature, 509, 63

Snik, F., Otten, G., Kenworthy, M., et al. 2012, in SPIE Astronomical Telescopes+ Instrumentation, 84500M–84500M

Sparks, W. B., & Ford, H. C. 2002, The Astrophysical Journal, 578, 543

Trinh, C. Q., Ellis, S. C., Bland-Hawthorn, J., et al. 2013, The Astronomical Journal, 145, 51

Wang, J., Mawet, D., Ruane, G., Hu, R., & Benneke, B. 2017, The Astronomical Journal, 153, 183